Bioinspired Hydrodynamic Force Feedforward for Autonomous Underwater Vehicle Control

Yiming Xu and Kamran Mohseni, *Senior Member, IEEE*

***Abstract*—It is believed that the lateral line found in most fish and some other aquatic organisms plays an important role in many behaviors by providing hydrodynamic information about the surrounding fluid. This paper presents a lateral line inspired feedforward control design for the autonomous underwater vehicles. The goal of this paper is to improve maneuvering accuracy for underwater exploration and environmental monitoring. The proposed controller takes pressure measurements at multiple locations over the entire vehicle hull and forms a B-spline surface approximation of the pressure distribution. Hydrodynamic forces acting on the vehicle are then estimated and passed to the controller for the improved trajectory tracking performance. The algorithm is formulated in such a way that the force estimation is a linear, fixed weight combination of the pressure signals, which enables rapid online computation. The performance of the feedforward controller is simulated in conjunction with the "robust integral of the sign of the error" control design. Trajectory tracking is investigated for control accuracy in the presence of localization errors. Reduced tracking errors are observed with the feedforward design. Experimental tests with pressure sensors on a moving cylinder further vindicate the force estimation algorithm.**

***Index Terms*—Feedforward systems, least squares methods, marine vehicles, surface fitting.**

I. Introduction

THE lateral line is a common mechanosensory system found in most fish and some other aquatic organisms [1], [2] (see Fig. 1). Considerable evidence suggests that it serves an important role in various behaviors including rheotaxis [3], schooling [4], prey detection and capture [5]–[7], and social communication [8]. The neuromast, a mechanoreceptive structure, is believed to be responsible for the functionality of the lateral line. Specifically, as illustrated in Fig. 1, superficial neuromasts located on the body surface and protruding into the external fluid respond to the direct-current and low-frequency components in the flow in proportion to the net velocity. Canal neuromasts situated in subdermal canals along the lateral lines respond to high-frequency components, and react proportionally to the net acceleration [7], [9], [10]. In effect, by detecting water motions and pressure gradients in the surrounding environment, the lateral line system provides hydrodynamic information that may facilitate many behavioral decisions.

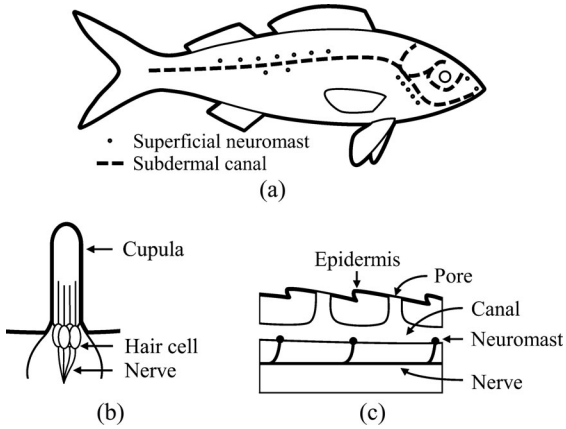

Fig. 1. Schematics of the lateral line system in a fish. (a) Typical layout of the lateral line in a fish. (b) Superficial neuromast. (c) Neuromasts in subdermal canal.

To date, several research groups have devoted their efforts to replicating the sensing capabilities of the lateral line. For example, in [11] and [12], designs of microfabricated artificial lateral line sensors are tested in dipole flow fields; in [13], pressure sensor arrays are used to identify the flow signature from static and moving cylinders with different cross sections; and in [14], parallel arrays of pressure sensors are deployed in the von Kármán vortex street to characterize the hydrodynamic signals for swimming control applications. In [15], a biomimetic design of the lateral line system was proposed, which utilizes commercially available pressure sensors to improve the maneuvering accuracy of the autonomous underwater vehicles (AUVs) for potential position holding, target tracking, docking, and other control tasks involved in the underwater exploration and environmental monitoring.

Traditionally, control performance of underwater vehicles is analyzed in static flow conditions with perturbations about some nominal traveling speed [16]. Hydrodynamic forces due to acceleration of the vehicle are modeled as added mass terms, as if some volume of fluid is moving together with the vehicle and causing an equivalent dissipative effect from the fact that the water is moving around it. Similarly, the viscous damping forces are expressed as functions of the vehicle's velocity, and influences from the nonstatic background flow are often considered as additional disturbances [16]. As long as the vehicle is operating with a dominant state of motion, the practice may

Manuscript received December 18, 2012; revised April 30, 2013; accepted June 11, 2013. Date of publication July 15, 2013; date of current version April 25, 2014. Recommended by Technical Editor D. G. Caldwell. This work was supported by the Office of Naval Research.

Y. Xu is with the Department of Mechanical and Aerospace Engineering, University of Florida, Gainesville, FL 32611 USA (e-mail: yxu@ufl.edu).

K. Mohseni is with the Department of Mechanical and Aerospace Engineering, Department of Electrical and Computer Engineering, and Institute for Networked Autonomous Systems, University of Florida, Gainesville, FL 32611 USA (e-mail: mohseni@ufl.edu).

Color versions of one or more of the figures in this paper are available online at http://ieeexplore.ieee.org.

Digital Object Identifier 10.1109/TMECH.2013.2271037

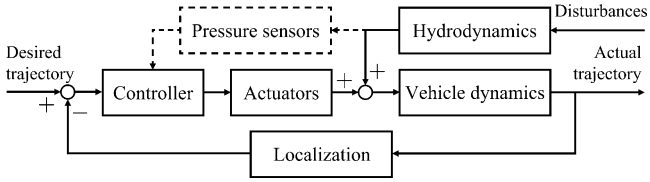

Fig. 2. Block diagram of vehicle control with pressure feedforward.

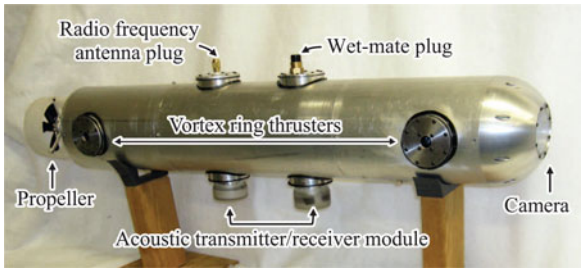

Fig. 3. CephaloBot prototype with cephalopod inspired VRTs.

result in a simple dynamic model, since the hydrodynamic forces are resolved into independent, linearly superposed terms. However, advances in high-maneuverability AUVs bring the need for accurate transition among different operation states and performing complex tasks with no dominant states, which requires a better model for the hydrodynamic forces.

Although accurate positioning is necessary to establish effective AUV control, underwater localization remains a challenging task as radio frequency communications (used by the global positioning system) are significantly attenuated and acoustic channels are affected by long propagation delays, limited bandwidth, and high bit error rates [17]. A variety of localization techniques have been developed for underwater applications (refer to a survey in [18]), but the position signals are generally subject to large errors in comparison to those of the surface vehicles. This further motivates the introduction of additional sensory systems to facilitate accurate AUV control.

Under the heuristic notion that the additional knowledge of the system's dynamics will improve the control performance, sensory information of the background flow may be helpful to overcome the aforementioned difficulties. As illustrated in Fig. 2, in addition to the standard feedback structure, the proposed control scheme includes a feedforward pathway that sends signals from the pressure sensors to the controller. Based on the readings, an approximation of the pressure distribution can be obtained. This gives an estimate of the total pressure force acting on the vehicle, which provides information on the added mass, velocity-based damping, and background flow disturbances. Therefore, modeling for the added mass and hydrodynamic damping terms becomes unnecessary. Furthermore, because information on the background disturbances is now available, better control performance may be expected.

The AUV model in this paper is based on the prototype CephaloBot developed by the group; see [19]. As shown in Figs. 3 and 4, the vehicle is equipped with cephalopod inspired vortex ring thrusters (VRTs) that can provide quantized propulsive force by creating arrays of high-momentum vortex rings

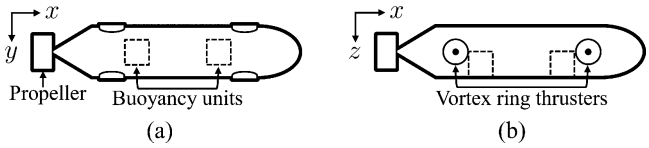

Fig. 4. Schematics of the propulsion system onboard CephaloBot. (a) Top view. (b) Front view.

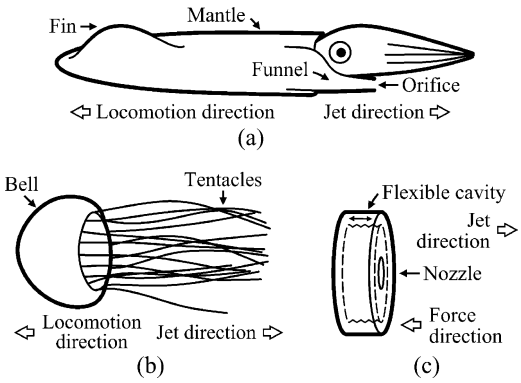

Fig. 5. Schematics of cephalopod locomotion and VRT propulsion. (a) Squid locomotion. (b) Jellyfish locomotion. (c) VRT propulsion.

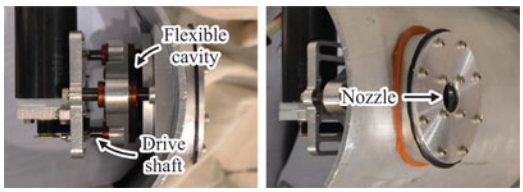

Fig. 6. Current design of VRTs onboard CephaloBot.

with successive ingestion and expulsion of water [20], [21] (illustrated in Figs. 5 and 6). The device allows the vehicle to perform accurate maneuvers at low speed, without sacrificing its low-drag streamline profile for efficient high-speed traveling [22]–[24]. It is worth mentioning that the feedforward control design described in this paper generally applies to all kinds of vehicles, yet it especially suits the need for improved maneuver accuracy on this particular type of underwater vehicle.

To investigate the advantages of the pressure feedforward configuration, trajectory tracking of the vehicle in the horizontal plane is simulated in comparison to a system without the feedforward element. A preliminary experimental test is conducted with the pressure sensors on an underwater cylinder to validate the hydrodynamic force estimation algorithm.

This paper is organized as follows. In Section II, a dynamic model of the vehicle is developed for the control design. Hydrodynamic force estimation and the control algorithm are presented in Sections III and IV, respectively. In Section V, simulation tests on the force estimation algorithm as well as the feedforward control design are illustrated, followed by the conclusion in Section VI. Proof of the control stability is provided in Appendix A. The experimental tests can be found in Appendix B.

II. Vehicle Dynamic Model

A. Kinematics

To describe the translational and rotational motions of the vehicle, a coordinate system in the body-fixed reference frame is defined with its origin at the geometric center of the vehicle; the x-axis points forward, the z-axis is directed from top to bottom, and the y-axis satisfies the right-hand rule, as shown in Fig. 4. For the motion in the horizontal plane, there are three degrees of freedom, namely, translational motions along x- and y-directions (surge and sway), and rotational motion about z-axis (yaw). At a time instant t, the vehicle's velocity is designated as vector $\boldsymbol{\nu}(t) \in \mathbb{R}^3$.

The earth-fixed reference frame is considered to be inertial, in which the earth-fixed coordinate system is defined with its x- and y-axes in the horizontal plane, and z-axis pointing downward. Position and orientation of the vehicle at a time instant t can be described in the earth-fixed frame as vector $\boldsymbol{\eta}(t) \in \mathbb{R}^3$. The velocity of the vehicle in the earth-fixed reference frame can be obtained by the following transformation:

$$\dot{\boldsymbol{\eta}} = \mathbf{J}(\boldsymbol{\eta})\,\boldsymbol{\nu} \tag{1}$$

where the matrix $\mathbf{J}(\boldsymbol{\eta}) \in \mathbb{R}^{3\times 3}$ is defined as

$$\mathbf{J}(\boldsymbol{\eta}) = \begin{bmatrix} \cos(\eta_3) & -\sin(\eta_3) & 0 \\ \sin(\eta_3) & \cos(\eta_3) & 0 \\ 0 & 0 & 1 \end{bmatrix}. \tag{2}$$

The variable $\eta_3(t) \in \mathbb{R}$ denotes the third component in the vector $\boldsymbol{\eta}(t)$, i.e., the angle of rotation about z-axis.

B. Kinetic Model

The dynamic equation for the vehicle can be written in the body-fixed frame as [16]

$$\boldsymbol{\tau} = \mathbf{M}\,\dot{\boldsymbol{\nu}} + \mathbf{C}(\boldsymbol{\nu})\,\boldsymbol{\nu} + \boldsymbol{f}_D + \boldsymbol{f}_N \tag{3}$$

where $\boldsymbol{\tau}(t) \in \mathbb{R}^3$ denotes the vector of control forces and moments from the actuators; matrices $\mathbf{M} \in \mathbb{R}^{3\times 3}$ and $\mathbf{C}(\boldsymbol{\nu}) \in \mathbb{R}^{3\times 3}$ denote the inertial terms and the Coriolis and centripetal terms, respectively; $\boldsymbol{f}_D(t) \in \mathbb{R}^3$ represents the vector of hydrodynamic damping forces and moments; and $\boldsymbol{f}_N(t) \in \mathbb{R}^3$ represents the unmodeled forces and moments.

To reiterate, the purpose of the feedforward design is to obtain an estimation for the hydrodynamic force $\widehat{\boldsymbol{f}}_D(t) \in \mathbb{R}^3$ using signals from the pressure sensors, in anticipation that the additional information will improve the control performance. Accordingly, the propulsive force $\boldsymbol{\tau}(t)$ combines the feedforward element $\widehat{\boldsymbol{f}}_D(t)$ with a feedback signal $\boldsymbol{\tau}_B(t) \in \mathbb{R}^3$ from any control design

$$\boldsymbol{\tau} = \boldsymbol{\tau}_B + \widehat{\boldsymbol{f}}_D. \tag{4}$$

Defining $\widetilde{\boldsymbol{f}}_D(t) \in \mathbb{R}^3$ to be the mismatch between the vector $\boldsymbol{f}_D(t)$ and its estimation $\widehat{\boldsymbol{f}}_D(t)$

$$\widetilde{\boldsymbol{f}}_D = \boldsymbol{f}_D - \widehat{\boldsymbol{f}}_D \tag{5}$$

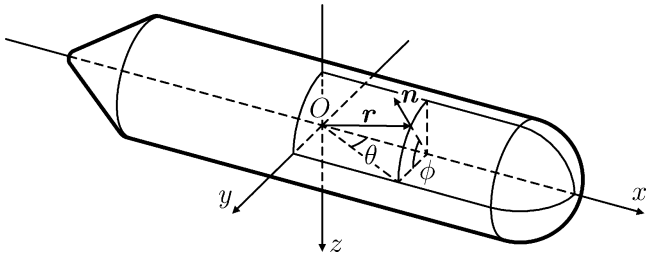

Fig. 7. Geometric model for describing the convex vehicle surface.

the equation of motion becomes

$$\boldsymbol{\tau}_B = \mathbf{M}\,\dot{\boldsymbol{\nu}} + \mathbf{C}(\boldsymbol{\nu})\,\boldsymbol{\nu} + \widetilde{\boldsymbol{f}}_D + \boldsymbol{f}_N \tag{6}$$

which presumably reduces the scale of uncertainties in the system as compared with that in (3).

III. Force Estimation

In the body-fixed coordinate system, a biparametric surface describes the boundary of the vehicle. The hydrodynamic damping forces and moments acting on the surface come from the linear and angular velocities and accelerations of the vehicle relative to the background fluid.

Using surface fitting techniques, the pressure readings from the sensors at multiple locations can be used to reconstruct the pressure distribution over the entire body. Thus, the total damping force and moment exerted on the vehicle can be estimated by integrating the pressure distribution over the vehicle profile (excluding the locations of the actuators). The resultant force estimation will take the form of linear, fixed weight combinations of the pressure measurements.

A. Geometric Model

As illustrated in Fig. 7, the profile of the vehicle is described in the body-fixed coordinate system. For a point on the vehicle's surface, the position vector $\boldsymbol{r} \in \mathbb{E}^3$ and the normal vector $\boldsymbol{n} \in \mathbb{E}^3$ can be written as

$$\boldsymbol{r} = (r_x,\, r_y,\, r_z), \quad \boldsymbol{n} = (n_x,\, n_y,\, n_z) \tag{7}$$

where r_x, r_y, and r_z are components in $\boldsymbol{r}$ along the x-, y-, and z-axes, respectively; similarly for n_x, n_y, and n_z.

In general, the boundary of the vehicle can be represented with a biparametric surface, and thus, any position on the surface is uniquely defined by specifying a pair of parameters. In this paper, all extruding parts on the vehicle are ignored for simplicity, which gives a convex vehicle surface on which positions are conveniently determined by angles $\theta \in [-\pi,\, \pi) \subseteq \mathbb{R}$ and $\phi \in [-\pi/2,\, \pi/2) \subseteq \mathbb{R}$. Specifically, for position $\boldsymbol{r}$, the azimuthal angle in coordinate system Oxy is designated as θ, which subtends from the positive x-axis to the orthogonal projection of $\boldsymbol{r}$ on the Oxy plane; and ϕ denotes the azimuth in coordinate system Oyz. As a result of the parameterization, vectors $\boldsymbol{r}$ and $\boldsymbol{n}$ are expressed as functions in θ and ϕ.

B. Pressure Surface Fitting

Suppose a number of $p = p_\theta\, p_\phi \in \mathbb{N}$ sensors are located on the surface of the vehicle (p_θ and p_ϕ in each of the corresponding directions). Each sensor takes measurement of the normal pressure $P_s \in \mathbb{R}$ at position $\theta_s,\, \phi_s \in \mathbb{R}$ ($s = 1,\, 2, \ldots,\, p$). Surface fitting over the pressure measurements will give an estimate of the pressure distribution $\widehat{P}(\theta,\, \phi) \in \mathbb{R}$.

A B-spline surface is used to model the pressure distribution due to its flexibility in the spline degree and smoothness, and its linear property that will become helpful for online computation. For $\mathcal{C}^{k-2}$ and $\mathcal{C}^{l-2}$ continuity in the θ- and ϕ-directions, respectively, a closed periodic B-spline surface (see [25], [26] for detail) is used as the approximation function, with orders of k and l (degree $k-1,\, l-1 \in \mathbb{N}$) in the θ- and ϕ-directions. Thus, the estimated distribution $\widehat{P}(\theta,\, \phi)$ can be written as

$$\widehat{P}(\theta,\, \phi) = \boldsymbol{N}^\top(\theta)\, \mathbf{B}\, \boldsymbol{M}(\phi) \tag{8}$$

where entries in matrix $\mathbf{B} \in \mathbb{R}^{n\times m}$ denote the control vertices of the B-spline surface,

$$\mathbf{B} = \begin{bmatrix} B_{1,1} & B_{1,2} & \cdots & B_{1,m} \\ B_{2,1} & B_{2,2} & \cdots & B_{2,m} \\ \vdots & \vdots & \ddots & \vdots \\ B_{n,1} & B_{n,2} & \cdots & B_{n,m} \end{bmatrix}. \tag{9}$$

The vector of the B-spline basis functions in the θ-direction, $\boldsymbol{N}(\theta) \in \mathbb{R}^n$, is defined as

$$\boldsymbol{N}(\theta) = \boldsymbol{N}_1(\theta) + \boldsymbol{N}_2(\theta) \tag{10}$$

in which $\boldsymbol{N}_1(\theta),\, \boldsymbol{N}_2(\theta) \in \mathbb{R}^n$ are

$$\boldsymbol{N}_1(\theta) = [\, N_{0,k}(\theta) \quad N_{1,k}(\theta) \quad \cdots \quad N_{n-1,k}(\theta)\,]^\top \tag{11a}$$

$$\begin{aligned} \boldsymbol{N}_2(\theta) = \big[& N_{n,k}(\theta) \quad N_{n+1,k}(\theta) \quad \cdots \quad N_{n-1+\lceil k/2\rceil,k}(\theta) \\ & 0 \quad \cdots \quad 0 \quad N_{1-\lfloor k/2\rfloor,k}(\theta) \quad N_{2-\lfloor k/2\rfloor,k}(\theta) \\ & \cdots \quad N_{-1,k}(\theta)\big]^\top. \end{aligned} \tag{11b}$$

The basis function $N_{i,k}(\theta) \in \mathbb{R}$ is expressed with the recurrence formula due to [27]–[29]

$$N_{i,1}(\theta) = \begin{cases} 1, & \text{if } h_i \le \theta < h_{i+1} \\ 0, & \text{otherwise} \end{cases} \tag{12a}$$

$$N_{i,k}(\theta) = \frac{(\theta - h_i)\, N_{i,k-1}(\theta)}{h_{i+k-1} - h_i} + \frac{(h_{i+k} - \theta)\, N_{i+1,k-1}(\theta)}{h_{i+k} - h_{i+1}} \tag{12b}$$

and $h_i \in \mathbb{R}$ denotes the ith element of a knot vector with equal spacing of knots over the vehicle's outline

$$\begin{aligned} \int_{-\pi}^{h_i} \sqrt{r_x^2 + r_y^2}\, \mathrm{d}\theta = \frac{i}{n} \int_{-\pi}^{\pi} \sqrt{r_x^2 + r_y^2}\, \mathrm{d}\theta, \\ i = 1 - \lfloor k/2\rfloor,\, 2 - \lfloor k/2\rfloor, \ldots,\, n + \lceil k/2\rceil. \end{aligned} \tag{13}$$

The definition for basis function vector $\boldsymbol{M}(\phi) \in \mathbb{R}^m$ is analogous to $\boldsymbol{N}(\theta)$, and therefore omitted.

Based on the property for the Kronecker product (see [30]), the pressure estimation in (8) is equivalent to

$$\widehat{P}(\theta,\, \phi) = \boldsymbol{K}_{MN}^\top(\theta,\, \phi)\mathrm{vec}(\mathbf{B}) \tag{14}$$

where $\boldsymbol{K}_{MN}(\theta,\, \phi) \in \mathbb{R}^{mn}$ is the Kronecker product

$$\boldsymbol{K}_{MN}(\theta,\, \phi) = \boldsymbol{M}(\phi) \otimes \boldsymbol{N}(\theta) \tag{15}$$

and $\mathrm{vec}(\cdot)$ denotes vectorization of a matrix as in [30].

Per surface fitting, the control vertices are approximated in the least squares sense, i.e., for a given set of measuring points, θ_s, ϕ_s, and P_s, $s = 1,\, 2, \ldots,\, p$, the following cost function is minimized:

$$\sum_{s=1}^{p} \Big(\widehat{P}(\theta_s,\, \phi_s) - P_s \Big)^2. \tag{16}$$

Substituting (8) into (16) and applying standard linear least squares approximation techniques (refer to [31], [32]) yields m-by-n equations, which in turn are formulated as

$$\mathbf{K}_{GH}\, \mathbf{K}_{GH}^\top \mathrm{vec}(\mathbf{B}) = \mathbf{K}_{GH}\, \boldsymbol{P} \tag{17}$$

where $\mathbf{K}_{GH} \in \mathbb{R}^{mn\times p}$ denotes the Khatri–Rao product for partitioned matrices from [33] (refer to an overview in [34])

$$\mathbf{K}_{GH} = \mathbf{G} * \mathbf{H} \tag{18}$$

and $\boldsymbol{P} \in \mathbb{R}^p$ is the vector of pressure measurements

$$\boldsymbol{P} = [\, P_1 \quad P_2 \quad \cdots \quad P_p\,]^\top. \tag{19}$$

In (18), $\mathbf{G} \in \mathbb{R}^{m\times p}$ and $\mathbf{H} \in \mathbb{R}^{n\times p}$ are columnwise partitioned matrices defined as

$$\mathbf{G} = [\, \boldsymbol{M}(\phi_1) \quad \boldsymbol{M}(\phi_2) \quad \cdots \quad \boldsymbol{M}(\phi_p)\,] \tag{20a}$$

$$\mathbf{H} = [\, \boldsymbol{N}(\theta_1) \quad \boldsymbol{N}(\theta_2) \quad \cdots \quad \boldsymbol{N}(\theta_p)\,]. \tag{20b}$$

In order to obtain the control vertices $\mathrm{vec}(\mathbf{B})$ from (17), the matrix $\mathbf{K}_{GH}\, \mathbf{K}_{GH}^\top$ needs to be invertible. This implies that within the influencing region for every vertex (i.e., in the patch where the basis function associated with the vertex is nonzero), there should exist at least one pressure sensor. Since a vertex affects k or l neighboring intervals divided by the control knots along the θ- or ϕ-direction, the pressure sensors should be spread across the vehicle profile. By prescribing a sensor distribution such that every control region will contain at least one sensor, the matrix $\mathbf{K}_{GH}\, \mathbf{K}_{GH}^\top$ is always nonsingular.

Solving (17) for the control vertices $\mathrm{vec}(\mathbf{B})$ gives

$$\mathrm{vec}(\mathbf{B}) = \mathbf{K}_P\, \boldsymbol{P} \tag{21}$$

where $\mathbf{K}_P \in \mathbb{R}^{mn\times p}$ is defined as

$$\mathbf{K}_P = (\mathbf{K}_{GH}\, \mathbf{K}_{GH}^\top)^{-1} \mathbf{K}_{GH}\,. \tag{22}$$

Substituting (21) into the pressure estimates in (14) yields the fitting result

$$\widehat{P}(\theta,\, \phi) = \boldsymbol{K}_{MN}^\top(\theta,\, \phi)\, \mathbf{K}_P\, \boldsymbol{P}. \tag{23}$$

C. Estimation Model

Based on the fitting result, the damping force $\boldsymbol{F} \in \mathbb{E}^3$ and moment $\boldsymbol{M}_O \in \mathbb{E}^3$ relative to the origin O acting on the vehicle

are estimated by $\widehat{\boldsymbol{F}}$, $\widehat{\boldsymbol{M}}_O \in \mathbb{E}^3$, which can be written as double integrals over the 2-D domain $\mathcal{T} = [-\pi,\, \pi) \times [-\pi/2,\, \pi/2) \subseteq \mathbb{R}^2$

$$\widehat{\boldsymbol{F}} = \int\int_{\mathcal{T}} -\boldsymbol{n}\, \widehat{P}(\theta,\, \phi)\, r^2\, \mathrm{d}\theta\, \mathrm{d}\phi \tag{24a}$$

$$\widehat{\boldsymbol{M}}_O = \int\int_{\mathcal{T}} -\boldsymbol{r} \times \boldsymbol{n}\, \widehat{P}(\theta,\, \phi)\, r^2\, \mathrm{d}\theta\, \mathrm{d}\phi \tag{24b}$$

where $r = \|\boldsymbol{r}\| \in \mathbb{R}$ is the norm of the position vector $\boldsymbol{r}$, and the minus sign comes from the fact that the pressure is considered positive toward the vehicle surface.

For planar motions, the vector of estimated damping forces and moments $\widehat{\boldsymbol{f}}_D \in \mathbb{R}^3$ consists of the forces along the x- and y-directions, and the moment about the z-axis

$$\widehat{\boldsymbol{f}}_D = \begin{bmatrix} \widehat{F}_x & \widehat{F}_y & \widehat{M}_{Oz} \end{bmatrix}^\top. \tag{25}$$

Combined with (23) and (24), the force estimate $\widehat{\boldsymbol{f}}_D$ can be expressed as

$$\widehat{\boldsymbol{f}}_D = \int\int_{\mathcal{T}} \boldsymbol{b}\, \boldsymbol{K}_{MN}^\top(\theta,\, \phi)\, r^2\, \mathrm{d}\theta\, \mathrm{d}\phi\, \mathbf{K}_P\, \boldsymbol{P} \tag{26}$$

where $\boldsymbol{b} \in \mathbb{R}^3$ is defined as

$$\boldsymbol{b} = -\begin{bmatrix} n_x & n_y & r_x\, n_y - r_y\, n_x \end{bmatrix}^\top. \tag{27}$$

With (26), the damping forces and moments can be estimated as the pressure signal vector $\boldsymbol{P}$ premultiplied by a matrix that is a function of the locations for the pressure sensors. Once the sensor locations are defined, the matrix can be obtained *a priori*. Since only matrix multiplication is required for online calculation, the force estimation can be rendered effortlessly by the onboard embedded system.

IV. Control Design

According to the dynamic model in (6), the system is subject to estimation mismatch in the hydrodynamic disturbances and unmodeled forces and moments, both of which are assumed to be $\mathcal{C}^2$ continuous and upper bounded by known constants. The control design in this paper is thus based on the "robust integral of the sign of the error" (RISE) technique (see [35] and [36]) in conjunction with backstepping (due to [37], [38]) to bridge the control design between the reference frames.

The position and velocity vectors $\boldsymbol{\eta}(t)$ and $\dot{\boldsymbol{\eta}}(t)$ are assumed to be measurable. The velocity vector $\boldsymbol{\nu}(t)$ in the body-fixed frame can be obtained by using the transformation in (1). The control objective is to track a desired trajectory $\boldsymbol{\eta}_d(t) \in \mathbb{R}^3$ described with respect to the earth-fixed frame.

A. Position Error System

To quantify the tracking performance, position tracking error $\boldsymbol{e}_1(t) \in \mathbb{R}^3$ is defined as

$$\boldsymbol{e}_1 = \boldsymbol{\eta}_d - \boldsymbol{\eta}\,. \tag{28}$$

Taking time derivative of (28) gives the open-loop system for position error $\boldsymbol{e}_1(t)$

$$\dot{\boldsymbol{e}}_1 = \dot{\boldsymbol{\eta}}_d - \dot{\boldsymbol{\eta}} = \dot{\boldsymbol{\eta}}_d - \mathbf{J}(\boldsymbol{\eta})\, \boldsymbol{\nu}\,. \tag{29}$$

Using backstepping, the position error system in (29) is translated into the body-fixed reference frame for the control design of the motion dynamics in (6). A virtual desired velocity signal $\boldsymbol{\nu}_d(t) \in \mathbb{R}^3$ is designed to be

$$\boldsymbol{\nu}_d = \mathbf{J}^{-1}(\boldsymbol{\eta})\, (\dot{\boldsymbol{\eta}}_d + \alpha_1\, \boldsymbol{e}_1) \tag{30}$$

where $\alpha_1 \in \mathbb{R}$ denotes a positive constant control gain.

The backstepping error $\boldsymbol{e}_2(t) \in \mathbb{R}^3$ is defined to be the mismatch between the virtual desired velocity $\boldsymbol{\nu}_d(t)$ and the actual velocity $\boldsymbol{\nu}(t)$ in the body-fixed frame

$$\boldsymbol{e}_2 = \boldsymbol{\nu}_d - \boldsymbol{\nu}. \tag{31}$$

Substituting (30) and (31) into (29) yields the "closed-loop" system for position error $\boldsymbol{e}_1(t)$

$$\dot{\boldsymbol{e}}_1 = \mathbf{J}(\boldsymbol{\eta})\, \boldsymbol{e}_2 - \alpha_1\, \boldsymbol{e}_1\,. \tag{32}$$

B. Filtered Error System

To facilitate RISE-based control design, a filtered tracking error [39] $\boldsymbol{e}_3(t) \in \mathbb{R}^3$ is defined as

$$\boldsymbol{e}_3 = \dot{\boldsymbol{e}}_2 + \alpha_2\, \boldsymbol{e}_2 \tag{33}$$

where $\alpha_2 \in \mathbb{R}$ is a positive constant control gain. Substituting the definitions from (6), (30), and (31) into (33) yields the open-loop error system

$$\mathbf{M}\, \boldsymbol{e}_3 = \boldsymbol{\chi} + \widetilde{\boldsymbol{f}}_D + \boldsymbol{f}_N - \boldsymbol{\tau}_B \tag{34}$$

where $\boldsymbol{\chi}(t) \in \mathbb{R}^3$ is defined as

$$\boldsymbol{\chi} = \mathbf{M}\, \dot{\mathbf{J}}^{-1}(\boldsymbol{\eta}, \boldsymbol{\nu})\, (\dot{\boldsymbol{\eta}}_d + \alpha_1\, \boldsymbol{e}_1) + \mathbf{M}\, \mathbf{J}^{-1}(\boldsymbol{\eta})\, (\ddot{\boldsymbol{\eta}}_d + \alpha_1\, \dot{\boldsymbol{e}}_1) + \mathbf{C}(\boldsymbol{\nu})\, \boldsymbol{\nu} + \alpha_2\, \mathbf{M}\, \boldsymbol{e}_2\,. \tag{35}$$

The control input $\boldsymbol{\tau}_B(t)$ is designed as a combination of a feedback linearization term and a RISE-based feedback term

$$\boldsymbol{\tau}_B = \boldsymbol{\chi} + \boldsymbol{\mu} \tag{36}$$

where $\boldsymbol{\mu}(t) \in \mathbb{R}^3$ denotes the RISE term as

$$\boldsymbol{\mu} = \alpha_3\, \boldsymbol{e}_2 - \alpha_3\, \boldsymbol{e}_2(0) + \boldsymbol{\sigma} \tag{37}$$

and signal $\boldsymbol{\sigma}(t) \in \mathbb{R}^3$ is designed to be

$$\dot{\boldsymbol{\sigma}} = \alpha_2\, \alpha_3\, \boldsymbol{e}_2 + \beta\, \mathrm{sgn}(\boldsymbol{e}_2) + \boldsymbol{e}_2, \quad \boldsymbol{\sigma}(0) = \mathbf{0}_{3\times 1}\,. \tag{38}$$

Positive constants $\alpha_3,\, \beta \in \mathbb{R}$ are control gains.

C. Stability Analysis

From the aforementioned design of the control signal, the following theorem can be established.

Theorem 1: The controller given in (36), (37), and (38) ensures that all signals are bounded and that the tracking error is regulated in a sense that

$$\lim_{t\to\infty} \boldsymbol{e}_1(t) = \mathbf{0}_{3\times 1} \tag{39}$$

provided that the control gains α_1, α_2, α_3, and β (introduced in (30), (33), (37), and (38), respectively) are designed to be sufficiently large.

Proof of the theorem and further requirements for the control gains can be found in Appendix A. In the following sections, a

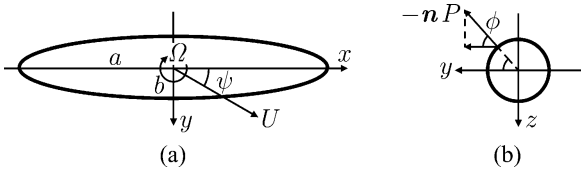

Fig. 8. Schematics of the vehicle's hydrodynamic model. (a) Top view. (b) Right side view.

series of simulation tests are conducted in regard to the proposed feedforward control structure.

V. Simulation Tests

A. Hydrodynamic Model

In this simulation, a 2-D hydrodynamic model is developed using the potential flow theory and is then extended to 3-D space to provide a reference pressure distribution over the vehicle surface.

As shown in Fig. 8, for positions on the horizontal plane Oxy, the pressure values come directly from the hydrodynamic calculation on the ellipse, whose major and minor semiaxes are chosen as

$$a = 0.395 \text{ m}, \quad b = 0.076 \text{ m}. \tag{40}$$

The pressure value at a location off the plane is assumed to be the projection length of the normal pressure vector (with the same magnitude) on the Oxy plane.

In the hydrodynamic model, the flow around the vehicle is estimated by the potential flow theory, assuming the flow to be irrotational, incompressible, and inviscid. Using a Joukowski transformation, the elliptic model in the complex plane z_c is mapped to a circle with a radius of r in the ζ_c plane

$$z_c = \zeta_c + \frac{a^2 - b^2}{4\,\zeta_c}, \quad r = \frac{a+b}{2}. \tag{41}$$

The flow field parameters (the relative linear speed U at an angle of ψ, the angular speed Ω, and the associated time derivatives) are also transformed, allowing a complex potential to be obtained in the ζ_c plane where

$$w = -U\left(\zeta_c\, e^{-i\,\psi} + \frac{r^2}{\zeta_c}\, e^{i\,\psi}\right) - i\,\Omega\left(\zeta_c^2 - \frac{r^4}{\zeta_c^2}\right). \tag{42}$$

To account for the sharp corner where the vehicle's propeller is located, the Kutta condition is applied at the rear end of the ellipse by adding an additional term to the potential as

$$W = w + \frac{i\,\Gamma}{2\,\pi}\ln(\zeta_c) \tag{43}$$

in which Γ is determined such that the flow velocity at $\zeta_c = a$ is zero. With the potential W, the hydrodynamic pressure on the ellipse can be obtained using Bernoulli's equation

$$P = P_0 - \frac{1}{2}\,\rho\left|\frac{\mathrm{d}W}{\mathrm{d}z}\right| - \rho\,\frac{\partial \Re(W)}{\partial t} \tag{44}$$

where ρ denotes the density of water, P_0 denotes the hydrostatic pressure at the far field, and $\Re(\cdot)$ denotes the real part of a complex number. Examples of similar techniques can be found in [40] and [41].

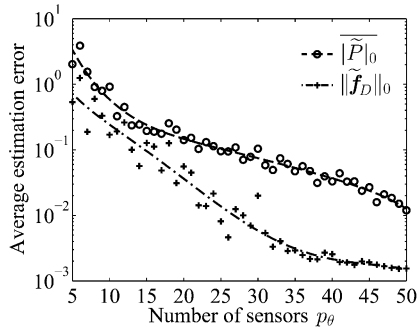

$\overline{|\widetilde{P}|_0}$: Mean relative pressure estimation error, averaged over runs
$\|\widetilde{f}_D\|_0$: Relative force estimation error, averaged over runs

Fig. 9. Relative error of pressure and force estimation versus number of sensors in θ-direction, averaged over runs with different hydrodynamic parameters.

B. Force Estimation

Fig. 9 shows the average pressure and force estimation errors over several sets of hydrodynamic parameters versus different sensor numbers p_θ in θ-direction. For each case, the number of control vertices n and the order k are chosen to give the minimal estimation error in the pressure distribution. It can be found from Fig. 9 that a reduced approximation error can be obtained with more pressure sensors. Under consideration of measurement accuracy of the pressure sensors, for the following control simulation, the sensor number p (p_θ and p_ϕ), the vertex numbers n and m, and the surface orders k and l are selected to be

$$\begin{aligned} &p_\theta = 20,\ n = 18,\ k = 3, \\ &p_\phi = 3,\ m = 2,\ l = 3\,. \end{aligned} \tag{45}$$

One of the reference pressure distributions and its estimation are illustrated in Fig. 10(a) and (b), respectively, with the following set of hydrodynamic parameters:

$$\begin{aligned} &U = 1 \text{ m/s}, \quad \psi = \pi/6 \text{ rad/s}, \quad \Omega = \pi/4 \text{ rad/s}, \\ &\dot{U} = 0.5 \text{ m/s}^2, \quad \dot{\psi} = \pi/100 \text{ rad/s}^2, \quad \dot{\Omega} = \pi/80 \text{ rad/s}^2 \end{aligned} \tag{46}$$

from which the vector of hydrodynamic damping forces and moments $\boldsymbol{f}_D(t)$ and its estimate $\widehat{\boldsymbol{f}}_D(t)$ are

$$\boldsymbol{f}_D(t) = [\,-93.50 \text{ N} \quad 5.37 \text{ N} \quad 3.65 \text{ N}\cdot\text{m}\,]^\top \tag{47a}$$

$$\widehat{\boldsymbol{f}}_D(t) = [\,-84.42 \text{ N} \quad 6.90 \text{ N} \quad 2.43 \text{ N}\cdot\text{m}\,]^\top. \tag{47b}$$

It should be noted that it is always possible to place the pressure sensors at locations where greater pressure gradients are expected. For example, as shown in Fig. 10(c), with careful choice of locations, a better force estimation can be achieved using fewer sensors ($p_\theta = 10$, $n = 9$, $k = 3$)

$$\widehat{\boldsymbol{f}}_D(t) = [\,-95.39 \text{ N} \quad 5.36 \text{ N} \quad 1.74 \text{ N}\cdot\text{m}\,]^\top. \tag{48}$$

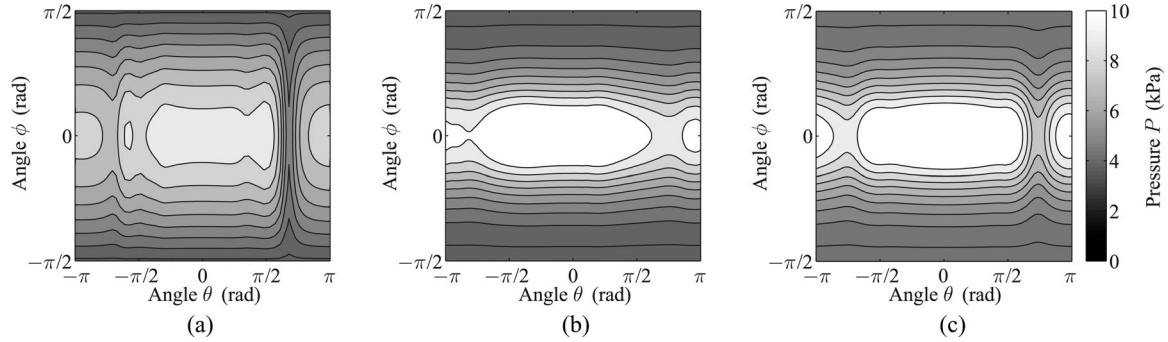

Fig. 10. Contour plot of the pressure distribution with hydrodynamic parameters in (46). (a) Reference distribution. (b) Estimation with uniform sensor locations. (c) Estimation with nonuniform sensor locations.

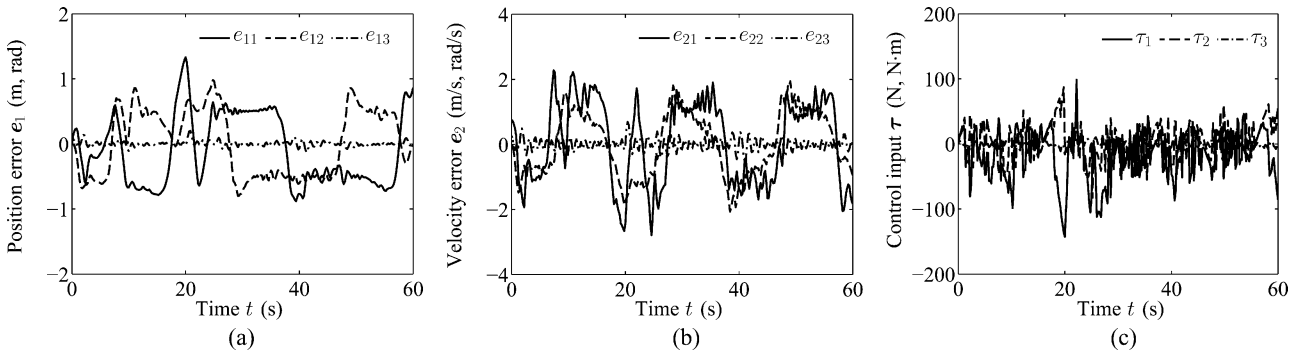

Fig. 11. Simulation result of trajectory tracking without the pressure feedforward. (a) Position error without pressure feedforward. (b) Velocity error without pressure feedforward. (c) Control input without pressure feedforward.

C. Control Simulation

The vehicle's acceleration relative to the background flow will affect the total hydrodynamic damping force and moment acting on the vehicle. This does not impose any complications in an actual system as long as the pressure sensors can provide trustworthy readings, but nevertheless, it creates difficulties for the simulation tests.

Since the total damping force contributes to the resultant force acting on the vehicle, based on which the acceleration of the vehicle is calculated, the fact that the damping force is a function of the relative acceleration produces a computational loop. In order to avoid solving hydrodynamic equations for the acceleration term, the effect from the relative acceleration on the damping force is ignored in this simulation. Although inaccuracies in the hydrodynamic force calculation may be resulted from the treatment, the simulation tests are still valid in terms of investigating the idea of using hydrodynamic force estimation to improve the control performance.

The inertia matrix $\mathbf{M}$ is expressed as

$$\mathbf{M} = \begin{bmatrix} p_1 & 0 & 0 \\ 0 & p_1 & p_2 \\ 0 & p_2 & p_3 \end{bmatrix} \tag{49}$$

where parameters $p_1,\, p_2,\, p_3 \in \mathbb{R}$ are defined to be

$$p_1 = 20\,\text{kg}, \quad p_2 = 2\,\text{kg}\cdot\text{m}, \quad p_3 = 4\,\text{kg}\cdot\text{m}^2\,. \tag{50}$$

Correspondingly, the centripetal-Coriolis matrix $\mathbf{C}(\boldsymbol{\nu})$ equals

$$\mathbf{C}(\boldsymbol{\nu}) = \begin{bmatrix} 0 & 0 & -p_1\,\nu_2 - p_2\,\nu_3 \\ 0 & 0 & p_1\,\nu_1 \\ p_1\,\nu_2 + p_2\,\nu_3 & -p_1\,\nu_1 & 0 \end{bmatrix} \tag{51}$$

where $\nu_1,\, \nu_2,\, \nu_3 \in \mathbb{R}$ are components in velocity vector $\boldsymbol{\nu}$.

Localization error is accounted for with dead band zones and sinusoidal noises (with spans of 0.5 m, $\pi/180$ rad, 1 m/s, and $\pi/90$ rad/s). Velocities of the background flow are defined as 0.2 m/s along the x-direction and $0.3\,\cos(0.2\,\pi\,t)$ m/s along the y-direction in the earth-fixed coordinate system.

The control gains are designed to be

$$\alpha_1 = \alpha_2 = \alpha_3 = 2, \quad \beta = 30. \tag{52}$$

Desired trajectory $\boldsymbol{\eta}_d(t)$ is designated as

$$\boldsymbol{\eta}_d(t) = \begin{bmatrix} 5\sin(0.15\,t) & \text{m} \\ 5 - 5\cos(0.15\,t) & \text{m} \\ 0.15\,t + 0.06 & \text{rad} \end{bmatrix} \tag{53}$$

which represents a horizontal circular orbit with a radius of 5 m, and a time period of about 42 s.

Simulation results, with and without the pressure feedforward, together with the hydrodynamic damping force are shown in Figs. 11–13, respectively. The control performances between the time interval from 20 to 60 s are compared in Table I.

Due to the existence of localization error, in which the controller is unable to acquire the actual position, the error does

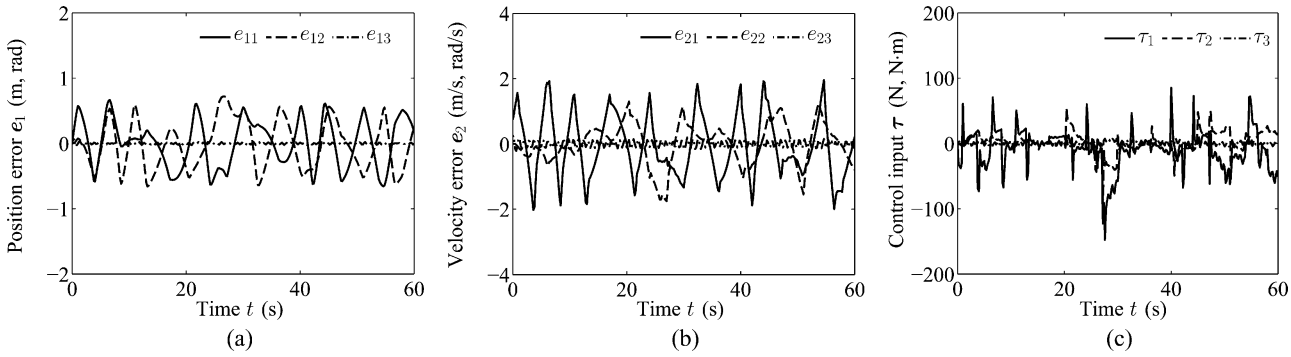

Fig. 12. Simulation result of trajectory tracking using the pressure feedforward. (a) Position error with pressure feedforward. (b) Velocity error with pressure feedforward. (c) Control input with pressure feedforward.

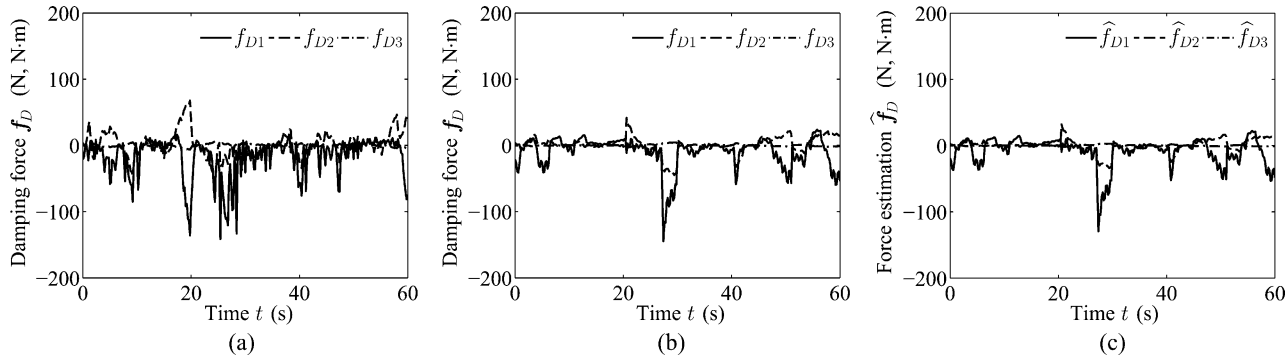

Fig. 13. Hydrodynamic damping force and its estimation for simulations with and without the pressure feedforward. (a) Damping force without pressure feedforward. (b) Damping force with pressure feedforward. (c) Force estimation with pressure feedforward

TABLE I
COMPARISON OF CONTROL PERFORMANCE FROM 20 TO 60 S

	Units	Without pressure feedforward		With pressure feedforward	
		Mean	Maximum	Mean	Maximum
Absolute	m	0.525	1.330	0.325	0.657
position	m	0.513	0.982	0.337	0.720
error	rad	0.029	0.204	0.010	0.035
Absolute	m/s	1.133	2.787	0.787	1.994
velocity	m/s	0.932	2.065	0.601	1.753
error	rad/s	0.148	0.694	0.079	0.196
Absolute	N	31.873	142.730	23.910	155.071
control	N	24.167	82.585	14.587	101.744
input	N·m	4.234	16.094	2.594	13.002

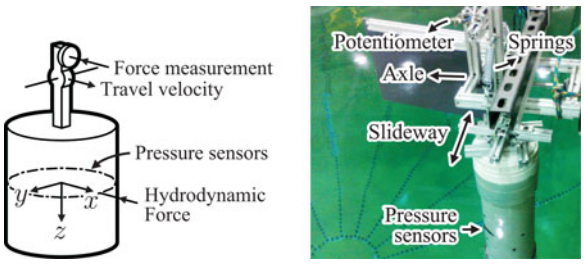

Fig. 14. Schematics and picture of the experiment setup.

not converge to zero in any of the tests, but is contracted within some bounding interval governed by the dead band spans and the control gains. However, since the system with the feedforward component can respond to hydrodynamic forces from the background flow, the only major disturbance affecting the control performance is the localization error. This may explain the absence of large deviations in the tracking errors compared to the system without the feedforward. Repeating the simulation using different sensor numbers demonstrates similar results. Generally, as long as the algorithm generates a fair estimation of the hydrodynamic force, the feedforward system exhibits about 20% to 50% less linear tracking error than the standard feedback system.

VI. CONCLUSION

Numerous studies have shown that the lateral line in fish and other aquatic organisms may provide valuable information of the surrounding underwater environment, which forms the basis for many behavioral decisions. In this paper, a lateral line inspired pressure feedforward design for underwater vehicle control is proposed to estimate hydrodynamic forces, which can be used to obtain a simple vehicle dynamic model without considering the added mass and viscous damping terms. The feedforward element also contains hydrodynamic information about the surrounding background flow that is traditionally categorized as unknown disturbance to the system. Therefore, the pressure feedforward design may serve as an important guidance for control maneuvers especially when there are uncertainties in localization.

Estimation of the hydrodynamic damping forces is obtained from measurements by arrays of pressure sensors located around the vehicle, with the help of least squares approximation to

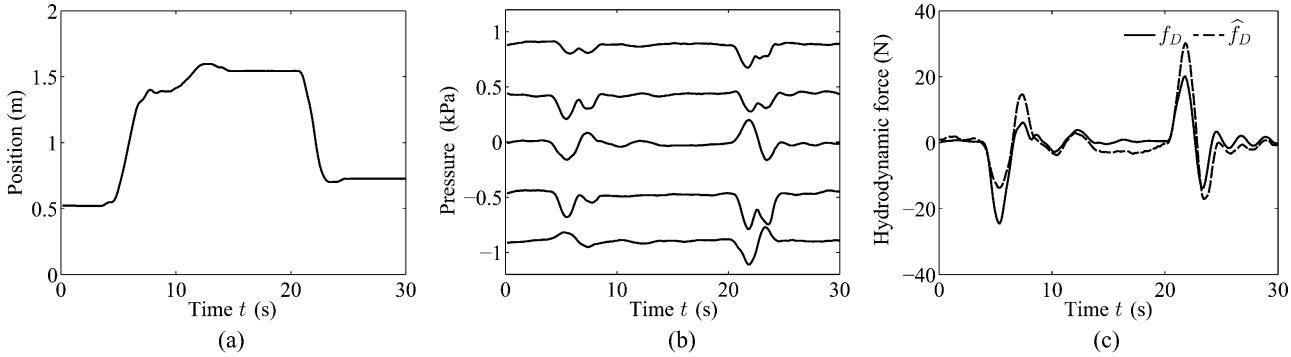

Fig. 15. Filtered signals and force estimation in experimental test. (a) Cylinder position. (b) Pressure signals. (c) Hydrodynamic force and its estimation.

reconstruct the pressure distribution as a closed periodic B-spline surface. The force estimate is then fed into the controller, completing the feedforward pathway in the control system as proposed in this paper. In agreement with the heuristic understanding, simulation tests indicate an improvement in control performance, especially in the presence of localization error and measurement noise.

Future work will be focused on implementation of the pressure feedforward design on the AUV. Moreover, since the pressure distribution around the vehicle may also be influenced by the vehicle's propulsion, information on the operation status of the actuators may be embedded in the pressure signals, which potentially can be used as propulsion feedback.

APPENDIX A
PROOF OF THEOREM 1

To facilitate subsequent analysis, from the definitions in (37) and (38), the time derivative for the RISE feedback signal $\boldsymbol{\mu}(t)$ is written as

$$\dot{\boldsymbol{\mu}} = \alpha_3\, \boldsymbol{e}_3 + \beta\, \mathrm{sgn}(\boldsymbol{e}_2) + \boldsymbol{e}_2\,. \tag{54}$$

Substituting the control input from (36) into (34) yields the closed-loop error system

$$\mathbf{M}\, \dot{\boldsymbol{e}}_3 = \widetilde{\boldsymbol{f}}_D + \boldsymbol{f}_N - \boldsymbol{\mu} \tag{55}$$

whose time derivative can be expressed as

$$\mathbf{M}\, \dot{\boldsymbol{e}}_3 = \boldsymbol{N}_B - \alpha_3\, \boldsymbol{e}_3 - \beta\, \mathrm{sgn}(\boldsymbol{e}_2) - \boldsymbol{e}_2 \tag{56}$$

where $\boldsymbol{N}_B(t) \in \mathbb{R}^3$ is defined as

$$\boldsymbol{N}_B = \dot{\widetilde{\boldsymbol{f}}}_D + \dot{\boldsymbol{f}}_N\,. \tag{57}$$

Several properties and assumptions are useful for the proof.

Property 1: The transformation matrix $\mathbf{J}(\boldsymbol{\eta})$ is orthogonal, and its Euclidean norm equals 1, i.e.,

$$\mathbf{J}^{-1}(\boldsymbol{\eta}) = \mathbf{J}^{\top}(\boldsymbol{\eta}), \quad \|\mathbf{J}(\boldsymbol{\eta})\| = \|\mathbf{J}^{\top}(\boldsymbol{\eta})\| = 1\,. \tag{58}$$

Property 2: The inertia matrix $\mathbf{M}$ is symmetric and positive definite. There exists positive constants $c_{M1},\, c_{M2} \in \mathbb{R}$ such that $\forall\, \boldsymbol{\varepsilon} \in \mathbb{R}^3$

$$c_{M1}\, \boldsymbol{\varepsilon}^{\top}\boldsymbol{\varepsilon} \leq \boldsymbol{\varepsilon}^{\top}\mathbf{M}\, \boldsymbol{\varepsilon} \leq c_{M2}\, \boldsymbol{\varepsilon}^{\top}\boldsymbol{\varepsilon}\,. \tag{59}$$

Assumption 1: The signal $\boldsymbol{N}_B(t)$ and its time derivative are bounded by known positive constants $c_1,\, c_2 \in \mathbb{R}$

$$\|\boldsymbol{N}_B(t)\| \leq c_1, \quad \|\dot{\boldsymbol{N}}_B(t)\| \leq c_2\,. \tag{60}$$

Proof: Define an auxiliary function $Q(t) \in \mathbb{R}$ to be

$$Q = \beta\, \|\boldsymbol{e}_2(0)\|_1 - \boldsymbol{e}_2^{\top}(0)\, \boldsymbol{N}_B(0) - L \tag{61}$$

where $L(t) \in \mathbb{R}$ is defined as

$$\dot{L} = \boldsymbol{e}_3^{\top}[\boldsymbol{N}_B - \beta\, \mathrm{sgn}(\boldsymbol{e}_2)], \quad L(0) = 0\,. \tag{62}$$

Substituting (33) into expression of L gives

$$\begin{aligned} L(t) &= \int_0^t \dot{\boldsymbol{e}}_2^{\top}(\zeta)\, \boldsymbol{N}_B(\zeta)\, \mathrm{d}\zeta - \int_0^t \beta\, \dot{\boldsymbol{e}}_2^{\top}(\zeta)\, \mathrm{sgn}(\boldsymbol{e}_{2(\zeta)})\, \mathrm{d}\zeta \\ &\quad + \int_0^t \alpha_2\, \boldsymbol{e}_2^{\top}(\zeta)\, [\boldsymbol{N}_B(\zeta) - \beta\, \mathrm{sgn}(\boldsymbol{e}_{2(\zeta)})]\, \mathrm{d}\zeta \\ &= [\boldsymbol{e}_2^{\top}(\zeta)\, \boldsymbol{N}_B(\zeta) - \beta\, \|\boldsymbol{e}_2(\zeta)\|_1]\big|_{\zeta=0}^{t} - \int_0^t \boldsymbol{e}_2^{\top}(\zeta)\, \dot{\boldsymbol{N}}_B(\zeta) \\ &\quad + \int_0^t [\boldsymbol{e}_2^{\top}(\zeta)\, \alpha_2\, \boldsymbol{N}_B(\zeta) - \alpha_2\, \beta\, \|\boldsymbol{e}_2(\zeta)\|_1]\, \mathrm{d}\zeta \\ &\leq \beta\, \|\boldsymbol{e}_2(0)\|_1 - \boldsymbol{e}_2^{\top}(0)\, \boldsymbol{N}_B(0) - (\beta - c_1)\, \|\boldsymbol{e}_2(t)\| \\ &\quad - \int_0^t (\alpha_2\, \beta - \alpha_2\, c_1 - c_2)\, \|\boldsymbol{e}_2(\zeta)\|\, \mathrm{d}\zeta\,. \end{aligned} \tag{63}$$

Thus,

$$Q(t) \geq (\beta - c_1)\, \|\boldsymbol{e}_2(t)\| + \int_0^t \alpha_2\, (\beta - c_1 - \frac{c_2}{\alpha_2})\, \|\boldsymbol{e}_2(\zeta)\|\, \mathrm{d}\zeta\,. \tag{64}$$

If β is designed such that

$$\beta \geq c_1 + \frac{c_2}{\alpha_2} \tag{65}$$

then

$$Q(t) \geq 0, \quad \forall\, t \geq 0\,. \tag{66}$$

Define signal $\boldsymbol{u}(t) \in \mathbb{R}^{10}$ as

$$\boldsymbol{u} = [\, \boldsymbol{e}_1^{\top} \quad \boldsymbol{e}_2^{\top} \quad \boldsymbol{e}_3^{\top} \quad \sqrt{Q}\,]^{\top}\,. \tag{67}$$

Let $\mathcal{D} \subset \mathbb{R}^{10}$ be a domain containing $\boldsymbol{u}(t) = \mathbf{0}_{10\times 1}$, and let $V(\boldsymbol{u}, t) : \mathcal{D} \times [0, \infty) \to \mathbb{R}$ be a continuously differentiable,

positive definite function as

$$V = \frac{1}{2}\boldsymbol{e}_1^\top \boldsymbol{e}_1 + \frac{1}{2}\boldsymbol{e}_2^\top \boldsymbol{e}_2 + \frac{1}{2}\boldsymbol{e}_3^\top \mathbf{M}\,\boldsymbol{e}_3 + Q \tag{68}$$

which satisfies

$$W_1(\boldsymbol{u}) \leq V(\boldsymbol{u}, t) \leq W_2(\boldsymbol{u})\,. \tag{69}$$

Functions $W_1(\boldsymbol{u})$, $W_2(\boldsymbol{u}) \in \mathbb{R}$ are continuous, positive definite, radially unbounded functions on $\mathcal{D}$ defined as

$$W_1(\boldsymbol{u}) = \frac{1}{2}\min\{1,\, c_{M1}\}\,\|\boldsymbol{u}\|^2 \tag{70a}$$

$$W_2(\boldsymbol{u}) = \frac{1}{2}\max\{1,\, c_{M2}\}\,\|\boldsymbol{u}\|^2\,. \tag{70b}$$

The time derivative of (68) can be written as

$$\begin{aligned}\dot{V} &= \boldsymbol{e}_1^\top \dot{\boldsymbol{e}}_1 + \boldsymbol{e}_2^\top \dot{\boldsymbol{e}}_2 + \boldsymbol{e}_3^\top \mathbf{M}\,\dot{\boldsymbol{e}}_3 + \dot{Q} \\ &= \boldsymbol{e}_1^\top \mathbf{J}(\boldsymbol{\eta})\,\boldsymbol{e}_2 - \alpha_1\,\|\boldsymbol{e}_1\|^2 - \alpha_2\,\|\boldsymbol{e}_2\|^2 - \alpha_3\,\|\boldsymbol{e}_3\|^2 \\ &\leq -W_3(\boldsymbol{u})\end{aligned} \tag{71}$$

where the function $W_3(u) \in \mathbb{R}$ is defined as

$$W_3(\boldsymbol{u}) = \min\left\{\alpha_1 - \frac{1}{2},\, \alpha_2 - \frac{1}{2},\, \alpha_3\right\}\,\|\boldsymbol{q}\|^2 \tag{72}$$

and $\boldsymbol{q}(t) \in \mathbb{R}^9$ is defined as

$$\boldsymbol{q} = [\,\boldsymbol{e}_1^\top \quad \boldsymbol{e}_2^\top \quad \boldsymbol{e}_3^\top\,]^\top\,. \tag{73}$$

Provided that $\alpha_1 > 1/2$ and $\alpha_2 > 1/2$, any choice of the domain $\mathcal{D} \subset \mathbb{R}^{10}$ will ensure the function $W_3(\boldsymbol{u})$ to be continuous and positive semidefinite on $\mathcal{D}$.

The inequalities in (69) and (71) can be used to show that $V(\boldsymbol{u}, t) \in \mathcal{L}_\infty$ in $\mathcal{D}$; hence, $\boldsymbol{e}_1(t), \boldsymbol{e}_2(t), \boldsymbol{e}_3(t) \in \mathcal{L}_\infty$ in $\mathcal{D}$. Due to the boundedness of the desired trajectory and its derivatives, one can show from (28), (30), (31), (32), and (33) that $\boldsymbol{\eta}(t), \boldsymbol{\nu}_d(t), \boldsymbol{\nu}(t), \dot{\boldsymbol{e}}_1(t), \dot{\boldsymbol{e}}_2(t) \in \mathcal{L}_\infty$ in $\mathcal{D}$; thus, $\boldsymbol{e}_1(t)$ and $\boldsymbol{e}_2(t)$ is uniformly continuous in $\mathcal{D}$. With (36), (37), and (38), it is obvious now that the control torque $\boldsymbol{\tau}(t) \in \mathcal{L}_\infty$ in $\mathcal{D}$. Therefore, using (56), one can show that $\dot{\boldsymbol{e}}_3(t) \in \mathcal{L}_\infty$ in $\mathcal{D}$; hence, $\boldsymbol{e}_3(t)$ is uniformly continuous in $\mathcal{D}$. From definitions in (72) and (73), function $W_3(\boldsymbol{u})$ is uniformly continuous in $\mathcal{D}$. Invoking [42, Th. 8.4] gives

$$\lim_{t\to\infty} W_3(\boldsymbol{u}_{(t)}) = 0, \quad \forall\, \boldsymbol{u}(0) \in \mathcal{D}\,. \tag{74}$$

From the fact that $W_3(\boldsymbol{u})$ asymptotically converges to zero, the global tracking result described in (39) can be obtained. ■

Remark 1: The differential equations in (56) and (62) have discontinuous right hand sides. However, the existence and uniqueness of the solution can still be shown according to [43] and [44], and is summarized in [45] for RISE-based controllers.

Remark 2: Although the stability analysis has proved a global result, it is often true that the unmodeled forces and moments are dependent on the system states, and hence, certain upper bounds for (60) might not hold globally, in which case the result reduces to be semiglobal.

APPENDIX B
EXPERIMENTAL TESTS

The force estimation algorithm is tested in experiment. In the setup shown in Fig. 14, an upright cylinder is rigidly fixed under a vertical beam along the z-axis, which is in turn pivoted about an axle in the y-direction that translates along a horizontal track in the x-direction. The cylinder is fully submerged under water with pressure sensors on the surface. At the other end of the beam, a spring structure and a linear potentiometer are installed to measure force. Scaled by the moment arm ratio, the force is compared to the pressure-based estimation.

In this test, five ME755 160 kPa gauge sensor are arranged horizontally on the surface of the cylinder with equal intervals. An MB1030 range sonar is used to register the position of the cylinder. In each test, the system starts from rest and accelerates to a constant speed before it decelerates back to a stop. The pressure distribution is assumed to be uniform along the vertical direction. Voltage signals gathered from the sensors are filtered with temporal averaging techniques to remove the noise. The data are converted to physical values with conversion ratios from calibration. For the pressure signals, the hydrostatic pressure in each sensor is obtained by taking the mean value during the time period when the system is stationary, and is subtracted from the pressure signal. Filtered and calibrated signals together with the force estimation from one of the tests are shown in Fig. 15. Pressure signals from the five sensors in Fig. 15(b) are vertically offset for better view. As can be seen in Fig. 15(c), the estimated force generally captures the variations in the measurement, which verifies the hydrodynamic force estimation algorithm. Consecutive tests arrive at the same conclusion.

ACKNOWLEDGMENT

The authors would like to thank the anonymous reviewers for their valuable comments and suggestions to improve the quality of this paper.

REFERENCES

[1] J. H. S. Blaxter, "Structure and development of the lateral line," *Biol. Rev.*, vol. 62, no. 4, pp. 471–514, Nov. 1987.
[2] H. Bleckmann, "Peripheral and central processing of lateral line information," *J. Comp. Physiol. A, Neuroethol. Sens. Neural Behav. Physiol.*, vol. 194, no. 2, pp. 145–158, Feb. 2008.
[3] J. C. Montgomery, C. F. Baker, and A. G. Carton, "The lateral line can mediate rheotaxis in fish," *Nature*, vol. 389, pp. 960–963, Oct. 1997.
[4] T. J. Pitcher, B. L. Partridge, and C. S. Wardle, "A blind fish can school," *Science*, vol. 194, no. 4268, pp. 963–965, Nov. 1976.
[5] J. C. Montgomery and J. A. Macdonald, "Sensory tuning of lateral line receptors in Antarctic fish to the movements of planktonic prey," *Science*, vol. 235, no. 4785, pp. 195–196, Jan. 1987.
[6] K. Pohlmann, J. Atema, and T. Breithaupt, "The importance of the lateral line in nocturnal predation of piscivorous catfish," *J. Exp. Biol.*, vol. 207, pp. 2971–2978, Aug. 2004.
[7] S. Coombs, C. B. Braun, and B. Donovan, "The orienting response of Lake Michigan mottled sculpin is mediated by canal neuromasts," *J. Exp. Biol.*, vol. 204, pp. 337–348, Jan. 2001.
[8] M. Satou, H. A. Takeuchi, J. Nishii, M. Tanabe, S. Kitamura, N. Okumoto, and M. Iwata, "Behavioral and electrophysiological evidences that the lateral line is involved in the inter-sexual vibrational communication of the himé salmon (landlocked red salmon, *Oncorhynchus nerka*)," *J. Comp.*

Physiol. A, Neuroethol. Sens. Neural Behav. Physiol., vol. 174, no. 5, pp. 539–549, May 1994.
[9] A. B. Kroese, J. M. van der Zalm, and J. van den Bercken, "Frequency response of the lateral-line organ of *Xenopus laevis*," *Pflugers Arch.*, vol. 375, no. 2, pp. 167–175, Jul. 1978.
[10] A. B. Kroese and N. A. Schellart, "Velocity- and acceleration-sensitive units in the trunk lateral line of the canal," *J. Neurophysiol.*, vol. 68, no. 6, pp. 2212–2221, Dec. 1992.
[11] Z. Fan, J. Chen, J. Zou, D. Bullen, C. Liu, and F. Delcomyn, "Design and fabrication of artificial lateral line flow sensors," *J. Micromech. Microeng.*, vol. 12, no. 5, pp. 655–661, Jun. 2002.
[12] Y. Yang, J. Chen, J. Engel, S. Pandya, N. Chen, C. Tucker, S. Coombs, D. L. Jones, and C. Liu, "Distant touch hydrodynamic imaging with an artificial lateral line," in *Proc. Nat. Acad. Sci. USA*, 2006, vol. 103, no. 50, pp. 18 891–18 895.
[13] V. I. Fernandez, A. Maertens, F. M. Yaul, J. Dahl, J. H. Lang, and M. S. Triantafyllou, "Lateral-line-inspired sensor arrays for navigation and object identification," *Mar. Technol. Soc. J.*, vol. 45, no. 4, pp. 130–146, Jul./Aug. 2011.
[14] R. Venturelli, O. Akanyeti, F. Visentin, J. Ježov, L. D. Chambers, G. Toming, J. Brown, M. Kruusmaa, W. M. Megill, and P. Fiorini, "Hydrodynamic pressure sensing with an artificial lateral line in steady and unsteady flows," *Bioinspir. Biomim.*, vol. 7, no. 3, pp. 1–12, Apr. 2012.
[15] Y. Xu, Z. Ren, and K. Mohseni, "Lateral line inspired pressure feedforward for autonomous underwater vehicle control," in *Proc. IEEE/RSJ IROS Workshop Robot. Environmental Monitor.*, Vilamoura, Portugal, Oct. 2012, pp. 1–6.
[16] T. I. Fossen, *Guidance and Control of Ocean Vehicles*. New York, NY, USA: Wiley, 1994.
[17] W. S. Burdic, *Underwater Acoustic System Analysis*, 2nd ed. Los Altos, CA, USA: Peninsula, 2003.
[18] H. P. Tan, R. Diamant, W. K. G. Seah, and M. Waldmeyer, "A survey of techniques and challenges in underwater localization," *Ocean Eng.*, vol. 38, no. 14-15, pp. 1663–1676, Oct. 2011.
[19] M. Krieg, P. Klein, R. Hodgkinson, and K. Mohseni, "A hybrid class underwater vehicle: Bioinspired propulsion, embedded system, and acoustic communication and localization system," *Mar. Technol. Soc. J.*, vol. 45, no. 4, pp. 153–164, Jul./Aug. 2011.
[20] K. Mohseni, "Zero-mass pulsatile jets for unmanned underwater vehicle maneuvering," presented at the 3rd AIAA Unmanned Unlimited Tech. Conf., Workshop Exhib., Chicago, IL, USA, Sep. 2004.
[21] K. Mohseni, "Pulsatile vortex generators for low-speed maneuvering of small underwater vehicles," *Ocean. Eng.*, vol. 33, no. 16, pp. 2209–2223, Nov. 2006.
[22] T. M. Thomas, M. Krieg, and K. Mohseni, "Thrust characterization for bioinspired pulsatile vortex ring thrusters with variable exit nozzle diameter," presented at the ASME Int. Mech. Eng. Congr. Expo., Buena Vista, FL, USA, Nov. 2009.
[23] M. Krieg and K. Mohseni, "Thrust characterization of pulsatile vortex ring generators for locomotion of underwater robots," *IEEE J. Ocean. Eng.*, vol. 33, no. 2, pp. 123–132, Apr. 2008.
[24] M. Krieg and K. Mohseni, "Dynamic modeling and control of biologically inspired vortex ring thrusters for underwater robot locomotion," *IEEE Trans. Robot.*, vol. 26, no. 3, pp. 542–554, Jun. 2010.
[25] L. A. Piegl and W. Tiller, *The NURBS Book*. New York, NY, USA: Springer-Verlag, 1997.
[26] D. F. Rogers, *An Introduction to NURBS: With Historical Perspective.*. San Mateo, CA, USA: Morgan Kaufmann, 2001.
[27] M. G. Cox, "The numerical evaluation of B-splines," *J. Inst. Math. Appl.*, vol. 10, no. 2, pp. 134–149, Oct. 1972.
[28] C. de Boor, "On calculating with B-splines," *J. Approx. Theory*, vol. 6, pp. 50–62, 1972.
[29] C. de Boor, *A Practical Guide to Splines*. New York, NY, USA: Springer-Verlag, 1978.
[30] R. A. Horn and C. R. Johnson, *Topics in Matrix Analysis*. Cambridge, U.K.: Cambridge Univ. Press, 1991.
[31] J. L. Buchanan and P. R. Turner, *Numerical Methods and Analysis*. New York, NY, USA: McGraw-Hill, 1992.
[32] J. D. Hoffman and S. Frankel, *Numerical Methods for Engineers and Scientists*, 2nd ed. New York, NY, USA: Marcel Dekker, 2001.
[33] C. G. Khatri and C. R. Rao, "Solutions to some functional equations and their applications to characterization of probability distributions," *Sankhyā*, vol. 30, no. 2, pp. 167–180, Jun. 1968.
[34] S. Liu and G. Trenkler, "Hadamard, Khatri-Rao, Kronecker and other matrix products," *Int. J. Inform. Syst. Sci.*, vol. 4, no. 1, pp. 160–177, 2008.
[35] Z. Qu and J. Xu, "Model-based learning controls and their comparisons using Lyapunov direct method," *Asian J. Control*, vol. 4, no. 1, pp. 99–110, Mar. 2002.
[36] B. Xian, D. M. Dawson, M. S. de Queiroz, and J. Chen, "A continuous asymptotic tracking control strategy for uncertain nonlinear systems," *IEEE Trans. Autom. Control*, vol. 49, no. 7, pp. 1206–1211, Jul. 2004.
[37] P. V. Kokotovic, "The joy of feedback: Nonlinear and adaptive," *IEEE Control Syst. Mag.*, vol. 12, no. 3, pp. 7–17, Jun. 1992.
[38] R. Lozano and B. Brogliato, "Adaptive control of robot manipulators with flexible joints," *IEEE Trans. Autom. Control*, vol. 37, no. 2, pp. 174–181, Feb. 1992.
[39] F. L. Lewis, C. T. Abdallah, and D. M. Dawson, *Control of Robot Manipulators*. New York, NY, USA: MacMillan, 1993.
[40] Z. Ren, D. Hall, and K. Mohseni, "A hybrid pseudo-spectral immersed-boundary method for applications to aquatic locomotion," presented at the 42nd AIAA Fluid Dyn. Conf., New Orleans, LA, USA, Jun. 2012, vol. 56, no. 18.
[41] X. Xia and K. Mohseni, "Axisymmetric synthetic jets: A momentum-based modeling approach," presented at the 42nd AIAA Fluid Dyn. Conf., New Orleans, LA, USA, Jun. 2012, vol. 56, no. 18.
[42] H. K. Khalil, *Nonlinear Systems*, 3rd ed. Englewood Cliffs, NJ, USA: Prentice-Hall, 2002.
[43] M. M. Polycarpou and P. A. Ioannou, "On the existence and uniqueness of solutions in adaptive control systems," *IEEE Trans. Autom. Control*, vol. 38, no. 3, pp. 474–479, Mar. 1993.
[44] Z. Qu, *Robust Control of Nonlinear Uncertain Systems*. New York, NY, USA: Wiley, 1998.
[45] P. M. Patre, W. MacKunis, M. Johnson, and W. E. Dixon, "Composite adaptive control for Euler-Lagrange systems with additive disturbances," *Automatica*, vol. 46, no. 1, pp. 140–147, 2010.

Yiming Xu received the B.S. degree in automation from Zhejiang University, Hangzhou, China, and the M.S. degree in mechanical engineering from the University of Florida, Gainesville, FL, USA, where he is currently working toward the Ph.D. degree.

His current research interests include dynamic modeling, nonlinear control design, and stability analysis of multiagent dynamic systems.

Kamran Mohseni (SM'10) received the B.S. degree from the University of Science and Technology, Tehran, Iran, the M.S. degree in aeronautics and applied mathematics from the Imperial College of Science, Technology and Medicine, London, U.K., and the Ph.D. degree in mechanical engineering from the California Institute of Technology (Caltech), Pasadena, CA, USA, in 2000.

He was a Postdoctoral Fellow in control and dynamical systems at Caltech for almost a year. In 2001, he joined the Department of Aerospace Engineering Sciences, University of Colorado at Boulder. In 2011, he joined the University of Florida, Gainesville, FL, USA, as the W.P. Bushnell Endowed Professor in the Department of Electrical and Computer Engineering and the Department of Mechanical and Aerospace Engineering. He is the Director of the Institute for Networked Autonomous Systems.

Dr. Mohseni is a member of the American Society of Mechanical Engineers, the American Physical Society, and the Society for Industrial and Applied Mathematics. He is an Associate Fellow of the American Institute of Aeronautics and Astronautics.